Joint cross-well and single-well seismic studies of CO$_2$ injection in an oil reservoir

R. Gritto,* T.M. Daley and L.R. Myer

Lawrence Berkeley National Lab, 1 Cyclotron Road, Mail Stop: 90-1116, Berkeley, CA 94720, USA

ABSTRACT

A series of time-lapse seismic cross-well and single-well experiments were conducted in a diatomite reservoir to monitor the injection of CO$_2$ into a hydrofracture zone, based on P- and S-wave data. A high-frequency piezo-electric P-wave source and an orbital-vibrator S-wave source were used to generate waves that were recorded by hydrophones as well as 3-component geophones. During the first phase the set of seismic experiments was conducted after the injection of water into the hydrofractured zone. The set of seismic experiments was repeated after a time period of seven months during which CO$_2$ was injected into the hydrofractured zone. The questions to be answered ranged from the detectability of the geological structure in the diatomic reservoir to the detectability of CO$_2$ within the hydrofracture. Furthermore, it was intended to determine which experiment (cross-well or single-well) is best suited to resolve these features.

During the pre-injection experiment, the P-wave velocities exhibited relatively low values between 1700 and 1900 m/s, which decreased to 1600–1800 m/s during the post-injection phase (-5%). The analysis of the pre-injection S-wave data revealed slow S-wave velocities between 600 and 800 m/s, while the post-injection data revealed velocities between 500 and 700 m/s (-6%). These velocity estimates produced high Poisson's ratios between 0.36 and 0.46 for this highly porous ($\sim 50\%$) material. Differencing post- and pre-injection data revealed an increase in Poisson's ratio of up to 5%. Both velocity and Poisson's ratio estimates indicate the dissolution of CO$_2$ in the liquid phase of the reservoir accompanied by an increase in pore pressure.

The single-well data supported the findings of the cross-well experiments. P- and S-wave velocities as well as Poisson's ratios were comparable to the estimates of the cross-well data.

The cross-well experiment did not detect the presence of the hydrofracture but appeared to be sensitive to overall changes in the reservoir and possibly the presence of a fault. In contrast, the single-well reflection data revealed an arrival that could indicate the presence of the hydrofracture between the source and receiver wells, while it did not detect the presence of the fault, possibly due to out-of-plane reflections.

INTRODUCTION

A subsurface CO$_2$ injection programme is currently operated by Chevron USA Production Company in the Lost Hills, California, oilfield (Fig. 1). This pilot programme, which is partially funded by the U.S. Department of Energy (DOE) as an enhanced oil recovery (EOR) project, is ideally suited for design and testing of geological sequestration concepts including subsurface monitoring techniques.

*E-mail: rgritto@lbl.gov

The reservoir at Lost Hills is comprised of diatomite, which consists of approximately equal parts of biogenic silica, clay and silty-sands. As the diatomite is buried at higher pressures and temperatures, the silica, which is initially in a form called opal-A, undergoes a phase transition to opal-CT and subsequently to quartz (Isaacs 1982; Bilodeau 1995). Hydrocarbons are found in all three phases with enhanced production from fracturing in transition zones. Depositional laminations in the diatomite with varying silica content affect the system permeability (Graham and Williams 1985). The layers with phase transitions may exhibit enhanced natural fracturing and therefore higher effective permeability, while other layers with lower permeability act as flow barriers.

The success of CO_2 sequestration will depend greatly on the reservoir properties. The diatomite reservoirs of central California have unusually high porosity (45–70%) and low permeability (<1 millidarcy). The pore size is <5 microns while the pore space is occupied by a mixture of water (50%), oil (45%) and gas (5%) (Perri *et al*. 2000). Because of the low permeability, the diatomite reservoir is developed with 5060 m^2 (1.25 acre) well spacing. Despite this small well spacing, only 5% of the estimated 2.6 billion barrels of oil in place has been produced since discovery in 1910. In the 1970s, the production of the Lost Hills oilfields was increased by the introduction of hydrofracturing to increase the reservoir permeability. In the 1990s, water floods were added as an enhanced oil recovery (EOR) technique. In 2000, Chevron

USA decided to start a CO_2 pilot project to study the applicability of this technique to the diatomaceous reservoir. Initial tests were successful, resulting in the recovery of 56–65% of the original oil in place (Perri *et al* 2000). Despite this success, the location and migration of the CO_2 was unknown, and thus it was decided to use seismic borehole methods to investigate whether the presence and the location of the CO_2 can be estimated.

Previous studies in carbonate reservoirs have shown that CO_2 injection causes seismic velocity changes, which can be spatially mapped using cross-well seismic surveys (Wang, Cates and Langan 1998). The seismic velocity changes can be up to 10%, which is easily detectable and mappable with modern cross-well seismic surveys. Therefore, borehole seismic surveys hold promise for mapping and long-term monitoring of sequestered CO_2.

Our goal is to investigate, through field testing, the suitability of cross-well and single-well seismic techniques for imaging subsurface CO_2 and for monitoring geological sequestration on a finer scale than can be achieved with seismic surface methods. In particular, it was intended to determine whether time-lapse effects can be detected by either method, and whether they are suited to detect a cross-cutting fault and the gas-filled hydrofracture. In a concurrent study, other investigators are combining electromagnetic and seismic methods and use a rock-properties model to estimate water and gas saturation changes, as well as pressure changes in the reservoir (Hoversten *et al*. 2003).

LOST HILLS CO$_2$ INJECTION SITE

The CO$_2$ injection project at Lost Hills is being operated by Chevron USA. The layout of the injection test is shown in Fig. 2. There are four adjacent patterns (10 120 m^2 (2.5 acre) each) with one injection well centred in each pattern. The reservoir volume around injection well 11-8WR is the target of the current seismic study. The data were acquired in observation wells, OB-C1 and OB-C2, at a reservoir depth between 425 and 640 m.

The injection well was hydraulically fractured and water flooding was conducted before it was decided to switch to CO$_2$ injection, to study the improvement in the rate of enhanced oil recovery (Perri *et al*. 2000). The CO$_2$ injection began in August 2000 at a relatively low flow rate of 3.5 million m^3 per day. The rate has been gradually increased to the current rate of 12.0 million m^3 per day per injection well. The injection pressure is held at 5.5–6.2 MPa, while the reservoir temperature is

about 41°C. The effect on seismic velocities and bulk density caused by the presence of CO$_2$ varies with pressure and temperature. In particular, the transition from liquid to gas phase has a dramatic effect on seismic properties as shown by Wang *et al*. (1998). This is a key point at the Lost Hills site where the injection pressure and temperature are such that a subsurface gas phase of CO$_2$ is expected. If such a gas phase is present, the seismic visibility and mappability should be enhanced. Previous cross-well and single-well seismic studies have shown the ability to detect a gas-bearing fracture (Majer *et al*. 1997).

SEISMIC DATA ACQUISITION

Pre-CO$_2$-injection survey

The first set of seismic borehole experiments was conducted in August 2000, before the end of the water flood. During this experiment, a suite of cross-well and single-well data sets
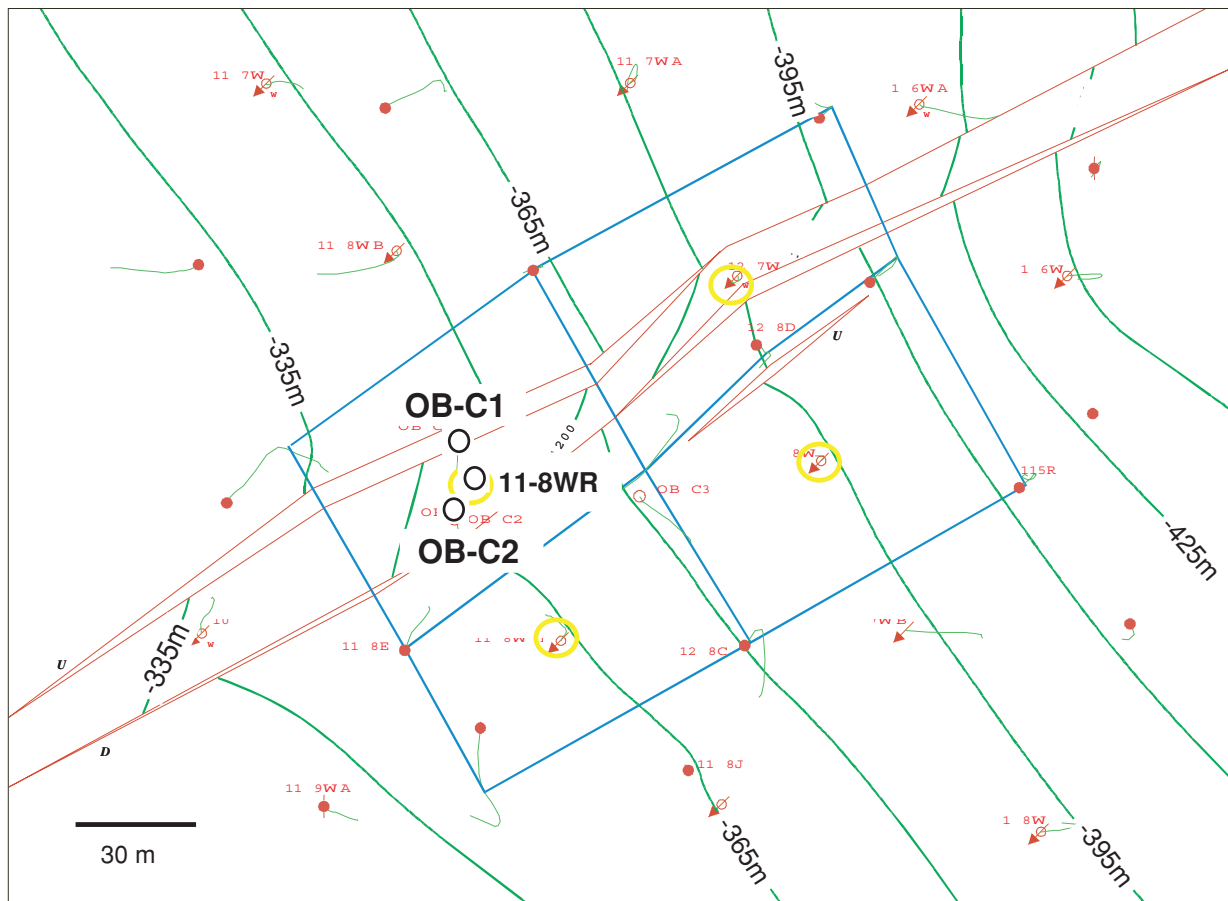

Figure 2 CO$_2$ injection site with the location of the injector (11-8WR) and the two observation wells (OB-C1 and OB-C2). The blue lines indicate the four injection patterns, while the green contour lines represent the top of the diatomic reservoir. The red lines are interpreted faults projected on to the top of the reservoir (from Chevron, USA).

were acquired using the observation wells, OB-C1 and OB-C2 (Fig. 2). The first survey used a high-frequency (800–3500 Hz) piezo-electric P-wave source in OB-C1 and a 3-component wall-locking accelerometer sensor in OB-C2. The second survey used an intermediate-frequency (70–350 Hz) orbital-vibrator source in OB-C1 recorded by the same receivers in OB-C2. The orbital vibrator wavefield can be reduced to two horizontal components of motion, in-line and transverse, with the latter generating mainly S-waves (Daley and Cox 2001). The third survey was a single-well imaging experiment in OB-C1 (i.e. source and receivers were placed in the same well) using the piezo-electric source and hydrophone sensors.

During the cross-well surveys, the sources and receivers covered a depth range from 400 m to 640 m, while the source and receiver spacing was 1.5 m (5 ft). The piezo-electric source
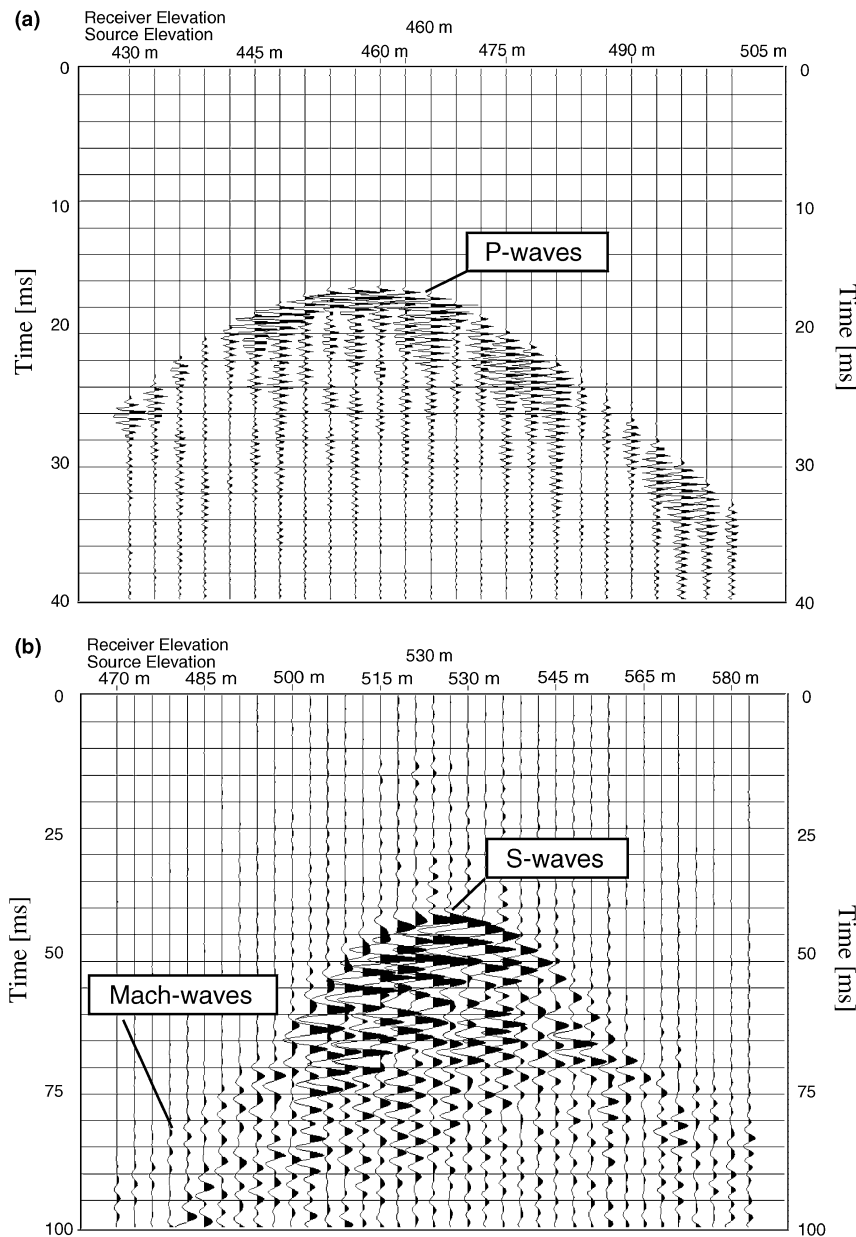
Figure 3 (a) Common-receiver gather (vertical component) at a depth of 460 m for the pre-injection cross-well experiment with the piezo-electric source. (b) Common-receiver gather at a depth of 530 m for the pre-injection cross-well experiment with the orbital-vibrator source (transverse horizontal component of source and receivers shown).

generated P-waves with a centre frequency of about 2000 Hz, which translates into wavelengths of about 1 m, while the orbital-vibrator source generates lower frequencies between 70 Hz and 350 Hz. However, because the S-wave velocities in the reservoir are relatively low (average of 650 m/s) and the maximum S-wave energy was observed at 250 Hz, the wavelength of the shear waves is about 2.6 m. Therefore, the spatial resolution of the two data sets is similar to first order, based on frequency considerations alone. We will address in the next paragraph the fact that the resolution of the S-wave data during the traveltime inversion is less than that of the P-wave data.

Figure 3 shows the vertical P-wave component of a common-receiver gather for the piezo-electric source (Fig. 3a) and the transverse horizontal S-wave component of a common-receiver gather of the orbital-vibrator source (Fig. 3b). The orbital-vibrator data have been processed to enhance the S-wave amplitudes while suppressing all other arrivals to facilitate the determination of S-wave arrival times. The P-wave in Fig. 3(a) shows a strong first arrival, although the waveforms appear to resonate after the onset of the wave. However, because of the strong signal-to-noise ratio, it was possible to determine the first-arrival times with good accuracy. The S-waves in Fig. 3(b) were more difficult to analyse. The data indicate that for zero-offset traces and traces at low angles of incidence, S-wave energy represents the first arrivals followed by tube waves, generated by wave conversion at the receiver well. For higher angles of incidence, a wave, indicated

as a Mach wave, is visible as the first arrival passing the S-wave energy. Mach waves are observed when the S-wave velocities in the medium are lower than the tube-wave velocity in the borehole. The Mach waves are generated by tube-wave energy travelling up and down the source well, radiating S-wave energy into the medium. These waves arrive at the receiver well with an apparent velocity faster than that of the S-waves in the medium velocity (Meredith, Toksöz and Cheng 1993). Therefore, the S-wave arrival times were only determined at low angles of incidence, which limited the spatial resolution of the velocity estimates in the S-wave traveltime inversion.

The single-well data, generated by the piezo-electric source, are shown in Fig. 4. The data were recorded with a 15-level hydrophone string with 1.5 m (5 ft) spacing. The data in Fig. 4 represent a common-offset gather, where the offset between the source and a single receiver is kept constant throughout the reservoir interval. For the case of a constant-velocity medium, the moveout would be horizontal throughout the displayed depth interval in Fig. 4. In contrast, variations in the arrival times would indicate variations in the medium velocity. Two groups of waves can be recognized in the data gather. These are the direct propagating P-waves arriving at about 19 ms, followed by tube-wave energy at about 26 ms. The large tube-wave amplitudes masked any energy present in the data that may have been reflected off the hydrofracture.

Technical problems prevented the acquisition of S-wave data in the pre-injection single-well experiment.

Figure 4 Common-offset gather of pre-injection single-well data generated with the piezo-electric source.
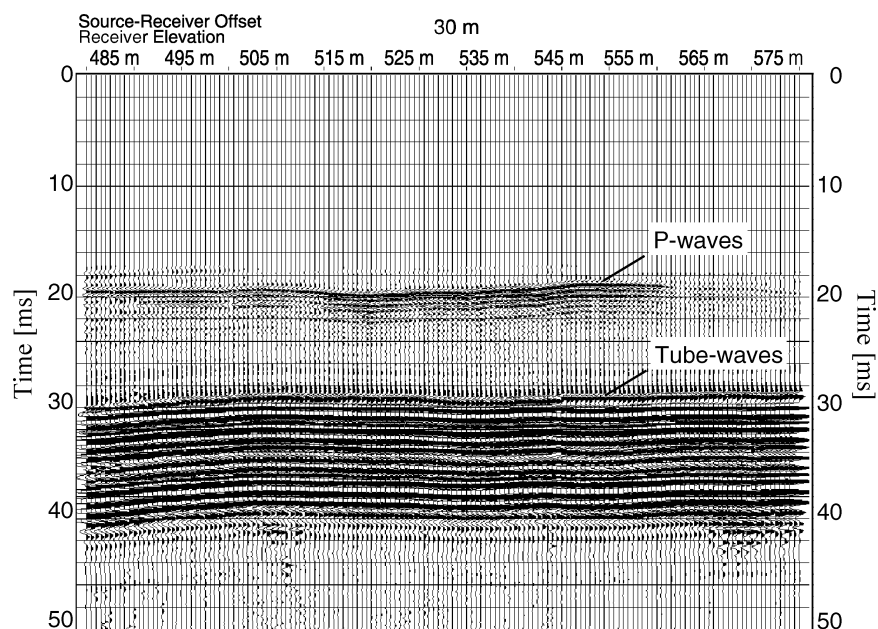
Post-CO₂-injection survey

The second set of seismic borehole experiments was conducted in May 2001, after a period of eight months of CO_2 injection. During this experiment a second suite of cross-well and single-well data sets was acquired using the same source combination as in the pre-injection experiment. However, technical problems with the sensors used in the pre-injection survey forced

us to deploy new hydrophones as receivers throughout the post-injection survey.

The post-injection cross-well data are shown in Fig. 5. The P-wave data generated with the piezo-electric source are presented in Fig. 5(a). It can be seen that the signal-to-noise ratio is comparable to the pre-injection data, and that the resonating character of the data is less pronounced. We attribute this observation to the use of a new hydrophone string in
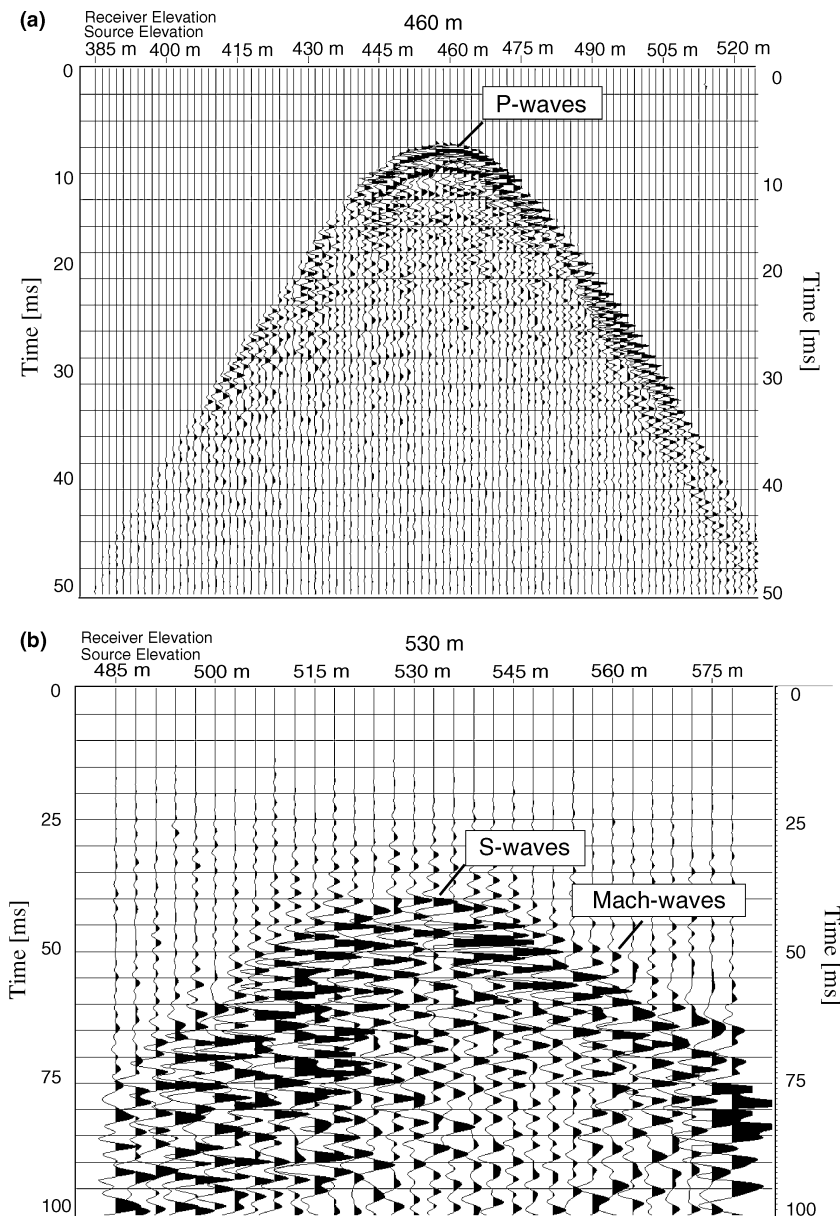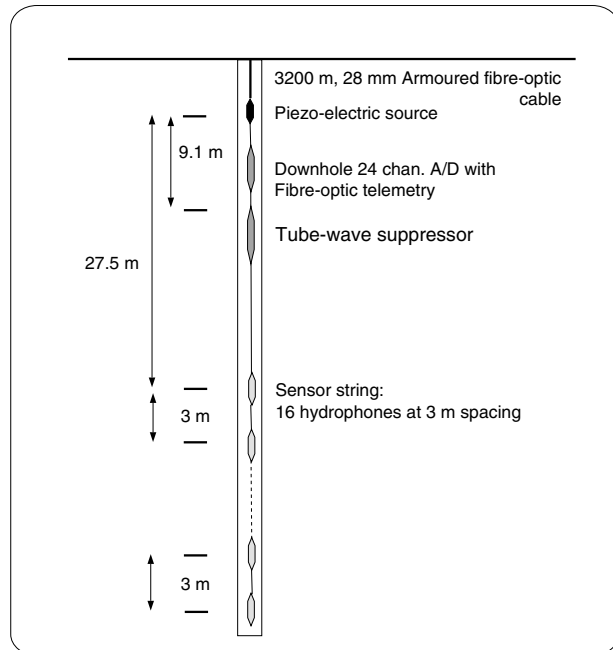

Figure 5 (a) Common-receiver gather at a depth of 460 m for the post-injection cross-well experiment with the piezo-electric source. (b) Common-receiver gather at a depth of 530 m for the post-injection cross-well experiment with the orbital-vibrator source.

the receiver well. The S-wave data generated with the orbital-vibrator source are shown in Fig. 5(b). Similarly to the pre-injection experiment, both S-wave and Mach waves can be seen in the common-receiver gather.

For the single-well experiment, a recently developed tool was introduced to attenuate the effect of the large tube-wave energy in the data. This tube-wave suppressor, designed by the Idaho National Engineering and Environmental Laboratory (INEEL), is placed between the source and the sensors as shown in Fig. 6. The figure depicts the single-well seismic-imaging equipment that is operated in a borehole to image the surrounding medium. A piezo-electric source is connected to a 3200 m fibre-optic wireline cable, with a 24-channel analogue-to-digital converter attached below. The digitizer converts the analogue input signal from the hydrophones to a digital output and sends it through the fibre-optic cable to a data recorder at the surface. The tube-wave suppressor is placed between the source and the hydrophones to attenuate energy propagating from the source along the borehole to the receivers below. The tube-wave suppressor contains a rubber bladder that is inflated with gas and kept slightly below the ambient pressure of the fluid column in the well. The tube waves, propagating past the suppressor, excite oscillations of the bladder and lose

their energy during this process (Daley *et al*. 2003a). This results in strongly attenuated tube waves relative to the body waves propagating through the medium outside the borehole. Figure 7 shows a common-offset gather for the single-well experiment using the tube-wave suppressor. The improvement over the data in Fig. 4 (single-well data without tube-wave suppressor) is apparent. The direct propagating P-wave is visible throughout the depth range of the reservoir, indicating velocity variations. There is only little tube-wave energy past the onset at 26 ms (compare with Fig. 4). Because of the attenuation of the tube waves, an additional arrival becomes apparent behind the direct P-wave at about 21 ms. This arrival will be interpreted in a later section. Unlike the pre-injection survey, an S-wave data set was acquired during the post-injection single-well experiment. The data are presented in Fig. 8. The results are similar to those in Fig. 7 in that the suppression of the tube-wave energy enabled the identification of the S-waves. The shear-wave arrival is visible between 37 ms and 52 ms revealing an increase in S-wave velocity with depth. Remnant tube-wave energy is visible between 25 ms and 35 ms, which would have overshadowed the weaker shear-wave arrival without tube-wave suppression. The P- and S-wave velocities from the single-well experiment will be analysed in a later section.

CROSS-WELL RESULTS

P-wave data

In order to determine velocity estimates of the reservoir, the first-arrival times for P- and S-waves were determined from the data. The traveltime data were inverted using a straight-ray back-projection algorithm (Peterson, Paulson and McEvilly 1985). The inversion process included static time shifts for each source and receiver location, to account for possible local anomalies around the borehole in the vicinity of sources and receivers, which could map into the velocity estimates if not corrected for.

The P-wave velocity estimates are shown in Fig. 9. The results are presented within the reservoir interval from 420 m to 640 m. The locations of the sources and receivers are denoted by stars and inverted triangles within the boreholes, OB-C1 and OB-C2, respectively. The geological layering is indicated by black lines, while the red line represents the location of an interpreted fault. Figure 9(a) represents the velocity estimates for the pre-injection experiment. It can be seen that the velocity varies slightly throughout the reservoir and increases with depth. An apparent transition from lower to higher
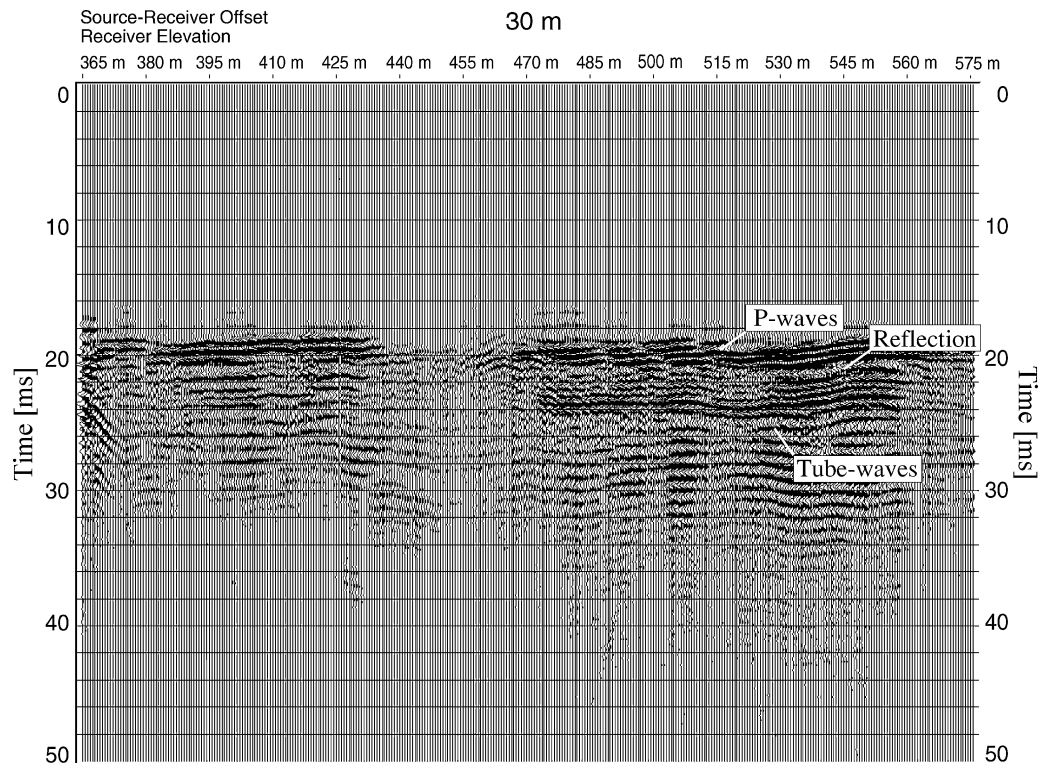

Figure 6 Single-well seismic data acquisition system. The sketch displays the system including piezo-electric source (which can be substituted by an orbital-vibrator source), downhole digitizer, tube-wave suppressor and hydrophones.

Figure 7 Common-offset gather of post-injection single-well data generated with the piezo-electric source. The suppression of tube-wave energy produced visible reflected energy.

velocities (1750–1850 m/s) can be seen at about 530 m depth, which is manifested by a change in lithology (Perri *et al*. 2000). Figure 9(b) shows the velocity estimates of the post-injection experiment. It can be seen that the overall velocity dropped about 50–80 m/s throughout the reservoir. The main velocity structure is similar to that of the pre-injection test with no apparent localized change in the pattern that could indicate the location of CO_2. For a better analysis of the temporal changes between the pre- and post-injection data, we compute the differences (post- minus pre-) between the two velocity tomograms. The results are shown in Fig. 9(c). The black dashes indicate the location of the injection intervals in the reservoir. It can be seen that the maximum velocity decrease is about 90 m/s (~5%), visible above the injection interval between 440 and 480 m depth, at an intermediate depth from 540 to 560 m, and in the lower part of the reservoir at 600 m depth. The top anomaly appears to be located between well OB-C2 and the fault, which seems to be partly inhibiting the extension of the anomaly towards well OB-C1. If this is a manifestation of the presence of CO_2, the gas must have migrated upwards above the fractured interval, caused by a possible extension of the fracture to shallower depth.

S-wave data

The pre-injection S-wave velocity estimates (Fig. 10a) corroborate the results of the P-wave data. The transition from upper to lower reservoir diatomite is clearly visible at about 530 m depth. Although the inversion resulted in very low S-wave velocity estimates between 550 and 850 m/s, these values are not uncommon for this soft reservoir rock (Bourbie, Coussy and Zinszner 1987; Morea 2002, pers. comm.). The S-wave velocity structure is similar to that of the P-waves with a low-velocity layer between 440 and 480 m, followed by intermediate velocities between 500 and 520 m depth, and a sharp transition to lower reservoir properties at 530 m depth. However, the spatial resolution of the S-wave data is limited by the predominantly subhorizontal ray coverage. The post-injection results in Fig. 10(b) reveal a velocity drop of about 50–80 m/s while the overall structure of the velocity image remains the same. Again, no apparent location of CO_2 is visible. The differenced results in Fig. 10(c) reveal a maximum decrease of 75 m/s (~9%) (the anomaly across the top of the image of −120 m/s is less reliable because of the limited ray coverage along the top of the reservoir, which was different for the
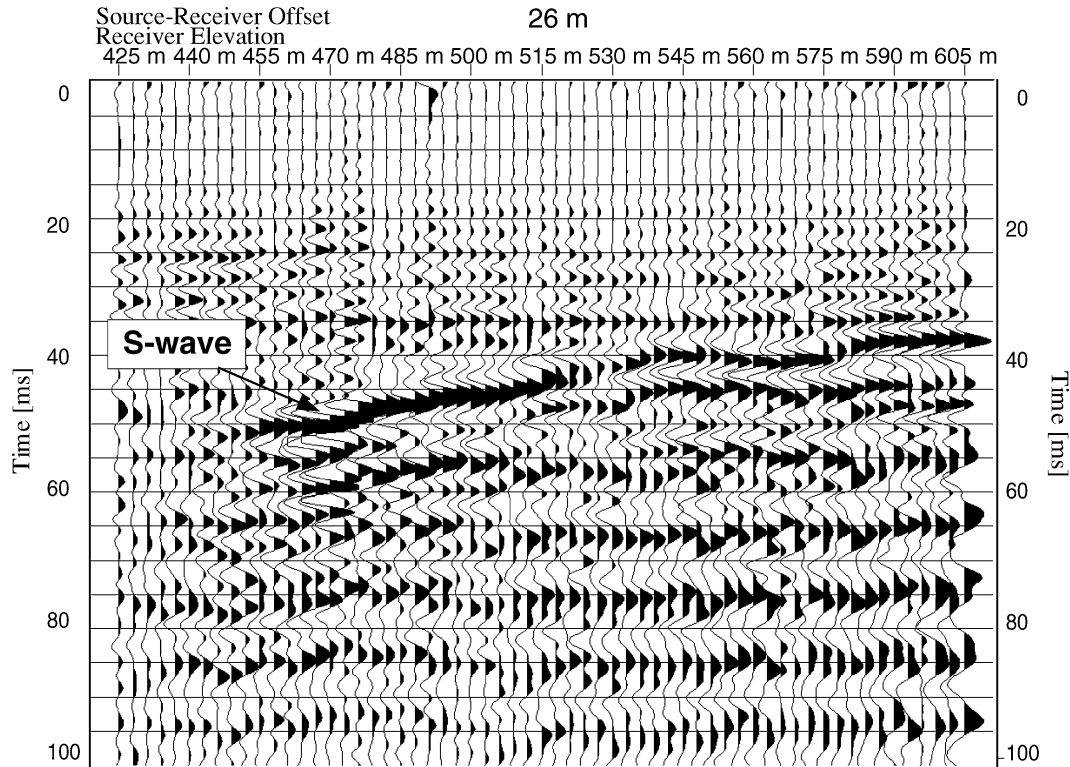
Figure 8 Common-offset gather of post-injection single-well data generated with the orbital-vibrator source. The suppression of tube-wave energy allowed the detection of the direct shear-wave arrival.

pre- and post-S-wave surveys). In comparison with the maximum P-wave velocity difference at 440–480 m between well OB-C2 and the fault, the S-wave velocities reveal an intermediate decrease of 60 m/s for the same location. However, in the central and bottom parts of the reservoir (560–580 m and 600 m depth), the S-wave velocity reveals decreased values comparable to those of the P-wave velocity.

The time-lapse velocity estimates for P- and S-waves show good correlation throughout the reservoir, although they represent independent data sets as they were excited by different seismic sources. At this point, however, the common interpretation does not yield a unique answer about the state of CO$_2$ in the reservoir. If CO$_2$ is present in gas form and the pore pressure does not change (i.e. gas displaces pore fluid), the P-wave velocity would decrease while the S-wave velocity would remain constant, as the S-wave is not sensitive to changes in gas or fluid saturation. However, since the S-wave velocities decrease, a pressure increase is likely to have occurred during the CO$_2$ injection phase. In this case, both P- and S-wave velocities would decrease since the differential pressure (confining-minus-pore pressure) would decrease. This scenario is possible for the case of free gas as well as for

the case of the dissolution of CO$_2$ into the liquid phase in the reservoir. To answer the question of the state of the CO$_2$ of the reservoir, we calculate Poisson's ratio and interpret the results in the next section.

Poisson's ratio

Poisson's ratio (PR) is calculated based on the velocity estimates for P- and S-waves shown in Figs 9 and 10 as

$$\nu = \frac{0.5(V_{\rm p}/V_{\rm s})^2 - 1}{(V_{\rm p}/V_{\rm s})^2 - 1}. \tag{1}$$

Figure 11(a) shows the PR for the pre-injection experiment. The estimates mimic the trend of the P- and S-wave velocity estimates. The PR shows a clear separation into the upper and lower reservoir diatomite with the transition at 530 m depth, as shown before. The high PR in the upper reservoir section is caused by the low S-wave velocity estimates. However, PRs of 0.42–0.45 are not uncommon for this highly porous rock (Bourbie *et al*. 1987). The decrease in PR with depth is an indication of the compaction of the diatoms accompanied by an increase in density (Bilodeau 1995).

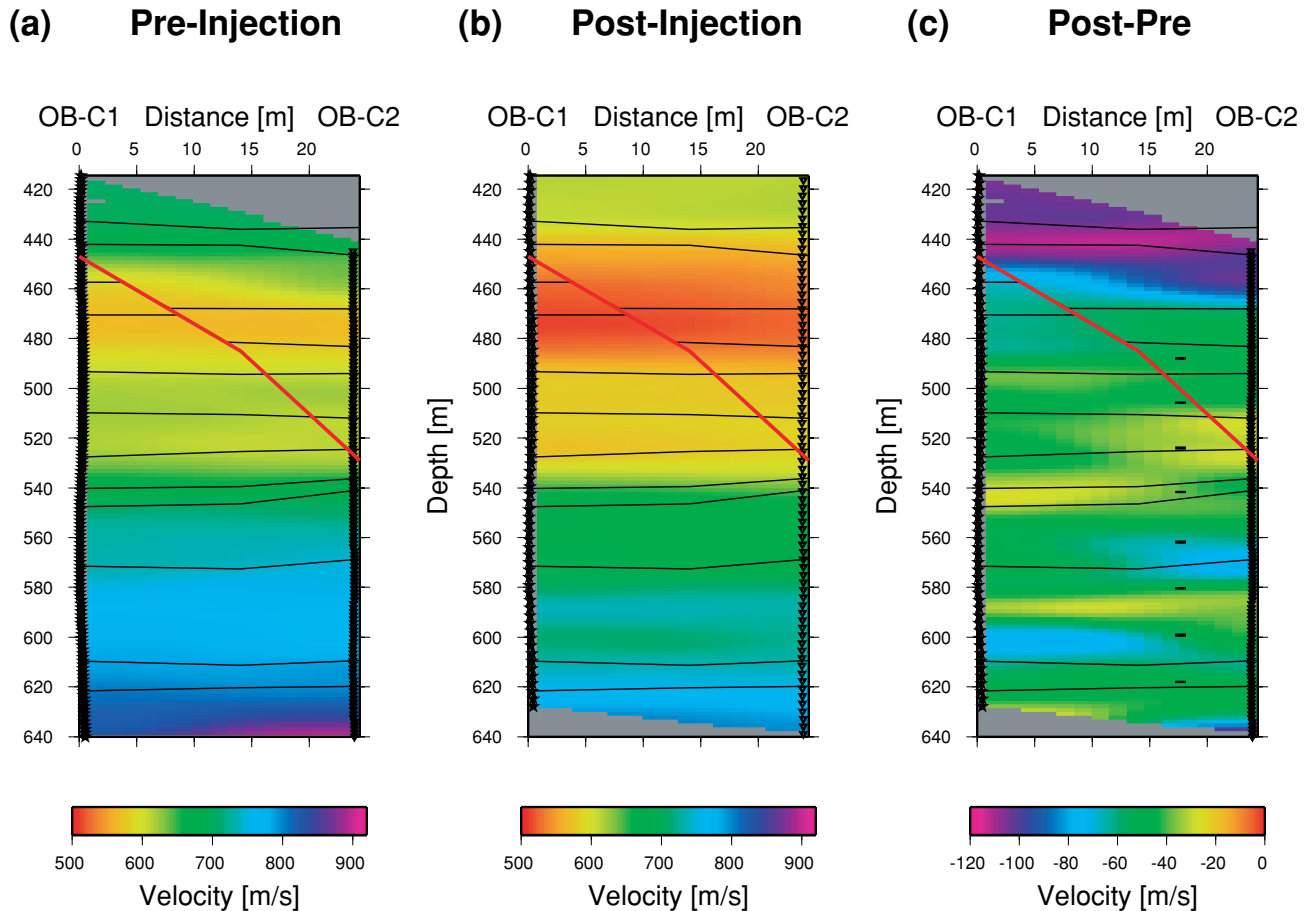**(a)   Pre-Injection**   **(b)   Post-Injection**   **(c)   Post-Pre**
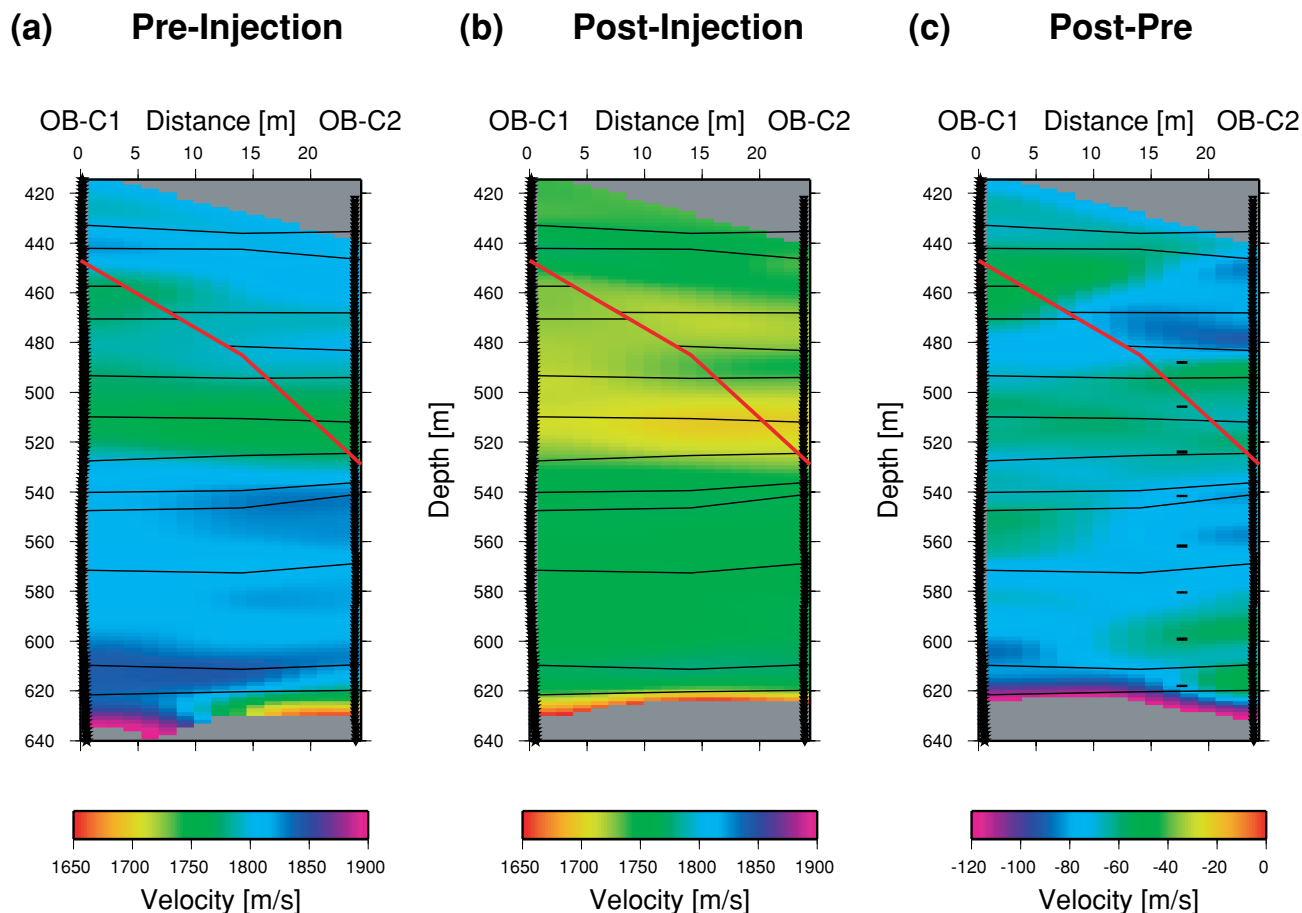
Figure 9 P-wave velocity estimates based on traveltime data. (a) Pre-injection estimates. (b) Post-injection estimates. (c) Result of differencing the post- and pre-injection estimates. The black dashes represent the projection of the CO_2 injection intervals on to the imaging plane.

The post-injection estimates (Fig. 11b) are similar to the pre-injection values, with the exception of higher values in the upper reservoir (440–460 m), where the S-wave velocities were particularly low.

The difference in PR is shown in Fig. 11(c). It can be seen that the time-lapse changes resulted in an increase in PR throughout the reservoir (the negative values at the bottom are an artefact of the inversion process caused by limited ray coverage). These results support the preliminary findings derived from the velocity inversions. If a free gas was present and the pore pressure increases (which is necessary in our case to explain the drop in S-wave velocity), the PR would decrease as shown by Dvorkin, Mavko and Nur (1999) and Mallick (2001). However, if the gas is in solution (i.e. the medium is fluid saturated) and the pore pressure increases, the PR increases as reported by Detournay and Cheng (1993), Dvorkin *et al.* (1999) and Simpson (2001). In a similar study, Dvorkin and Nur (1996) supported this conclusion by showing that

for water-saturated high-porosity sandstone (20–40%), the PR increases with decreasing confining pressure. To evaluate the estimates for the PR as shown in Fig. 11(c), we calculate the change in PR using a rock-properties model relating geophysical to reservoir parameters (Hoversten *et al.* 2003). The result is an increase in PR with an average value of 0.0045. In comparison, the average value of the increase in PR in Fig. 11(c) is 0.0074 ± 0.0052, yielding estimates in line with the prediction of the rock-properties model.

Thus a possible conclusion that can be drawn from the results of the PR is that CO_2 has dissolved into the liquid phase in the reservoir rock and increased the pore pressure in several compartments inside the reservoir. Figure 11(c) suggests that CO_2 migrated horizontally in the lower section of the reservoir around 570 and 600 m depth. The strong increase at the top of the reservoir above 440 m is probably an artefact resulting from low resolution of the S-wave estimates. However, the slight increase visible above the top of the injection

Figure 10 S-wave velocity estimates based on traveltime data. (a) Pre-injection estimates. (b) Post-injection estimates. (c) Result of differencing the post- and pre-injection estimates. The black dashes represent the projection of the CO_2 injection intervals on to the imaging plane.

interval may indicate an over-pressurization of the reservoir caused by an upward migration of the CO_2, as the PR should have remained constant otherwise. However, it is also possible that some of the regions that reveal an increase in PR have undergone a pore-pressure increase caused by the injection process, without the CO_2 actually reaching these zones.

In the following, the results of the cross-well experiment will be compared with the single-well data.

SINGLE-WELL RESULTS

Direct waves

A conceptual model of a single-well seismic experiment is shown in Fig. 12, where a source emits seismic energy, which propagates to receivers below (a reverse geometry where the source is located below the receivers has also been used for single-well imaging in the past). The direct waves reach fur-

ther into the medium compared with sonic logging because the source–receiver offset and the wavelengths of the waves are longer. At the same time, waves propagate outwards from the well and reflect off interfaces above and below, and off features such as faults and fractures that may be present in the medium.

The direct arrival times of the P-waves (pre- and post-injection) and the S-waves (post-injection) were determined from the single-well data collected in well OB-C1. The results are plotted in Fig. 13. The pre-injection results are shown in Fig. 13(a). The thick grey line represents the velocity measurements from the single-well data (plotted at the source–receiver midpoint), while the thin black line is an average cross-well tomographic velocity combining the estimates of the three pixels adjacent to the source well OB-C1 at each depth position (horizontal average over 5 m). Although static source corrections have been accounted for, the average yields a better comparison because the P-waves of the single-well data propagate

(a)   Pre-Injection   **(b)   Post-Injection**   **(c)   Post-Pre**
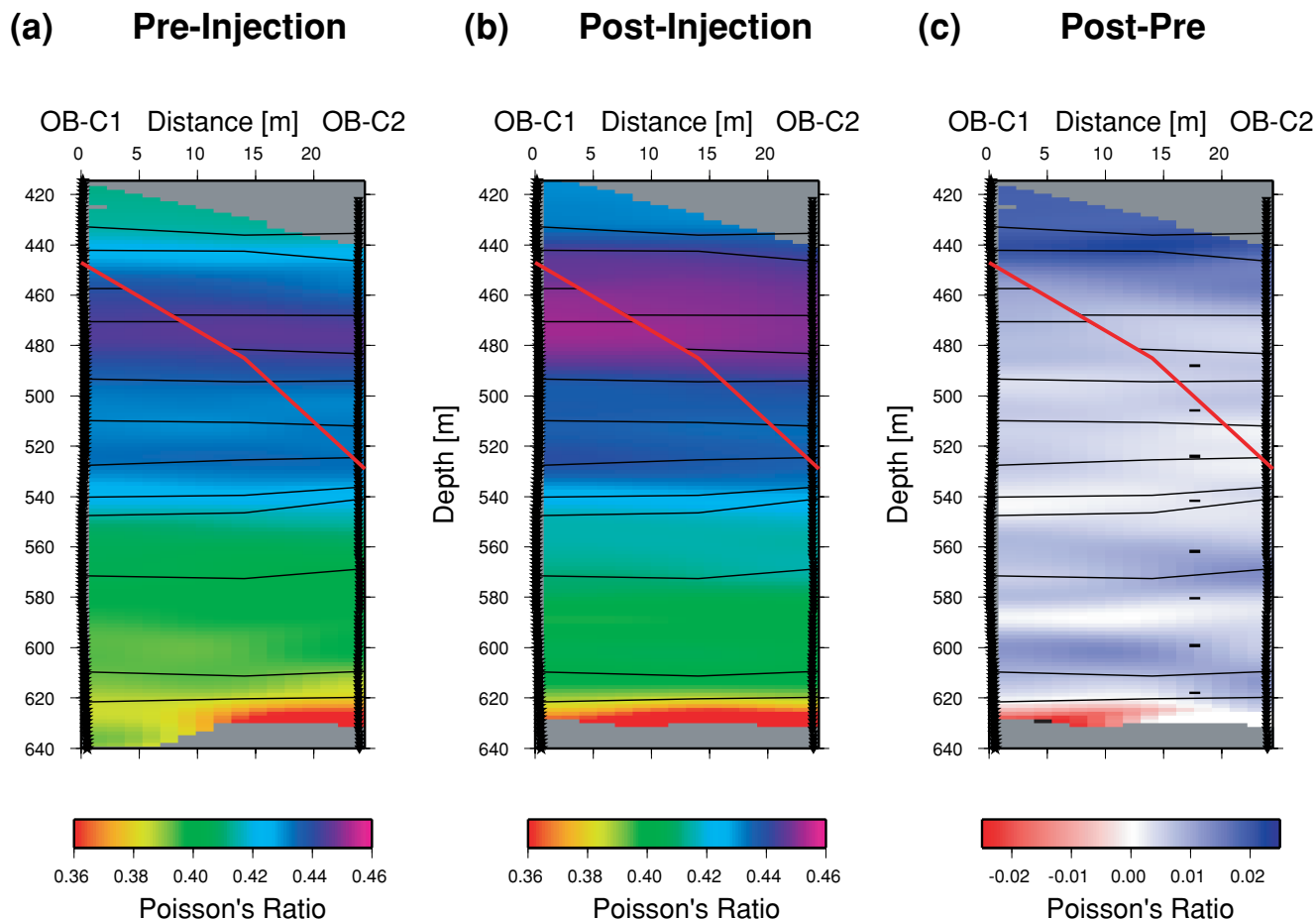

Figure 11 Poisson's ratio based on the P- and S-wave velocity estimates in Figs 9 and 10. (a) Pre-injection ratio. (b) Post-injection ratio. (c) Result of differencing the post- and pre-injection ratios. The black dashes represent the projection of the CO_2 injection intervals on to the imaging plane.

further out from the well. The different depth ranges plotted in Fig. 13 are the result of different acquisition intervals caused by different receiver strings and source–receiver offsets. The fit is good where the measurements overlap, indicating that the near-borehole effects (i.e. borehole cement, borehole annulus) present in many sonic-log velocity data play only a minor role in the present case as the longer wavelengths integrate the effects further away from the borehole. This result corroborates the velocity estimates of the traveltime inversion. The post-injection P-wave results are shown in Fig. 13(b). The dashed line represents results of ultrasonic velocity measurements by Chevron, USA, on cores taken 126 m west of the CO_2 injection site (Morea 2002, pers. comm.). The overall fit between the single- and cross-well results is good, although the single-well data did not cover the lowermost section of the reservoir. Although the ultrasonic P-wave velocity measurements reveal more variation throughout the depth range, the average values

fall within the range of the field measurements. The comparison of the cross- and single-well S-wave field data in Fig. 13(c) reveals a good fit even down to details in the velocity structure (i.e. velocity increase with depth, velocity inversion between 460 and 480 m depth). The ultrasonic results show higher values in the upper reservoir, while they match the field data in the lower reservoir section. Finally, the post-injection PR is plotted in Fig. 13(d). The result of the single-well experiment is limited to the depth range where post-P- and S-wave data overlap. However, even for this limited depth range, the fit between the two graphs representing the field data is very good, revealing an overall decrease in the PR with increasing reservoir depth. The lower values at the bottom of the reservoir are in accordance with the transition from diatomite to a more shaley rock, which exhibits a PR between 0.35 and 0.40. The PR of the core data was computed based on equation (1), using the ultrasonic velocities as shown in Figs 13(a)

and 13(b). As expected from the trend of the S-wave data, the fit is better in the lower half of the reservoir.

The results suggest that the ultrasonic velocities and hence the PR are comparable to the values estimated from field data.
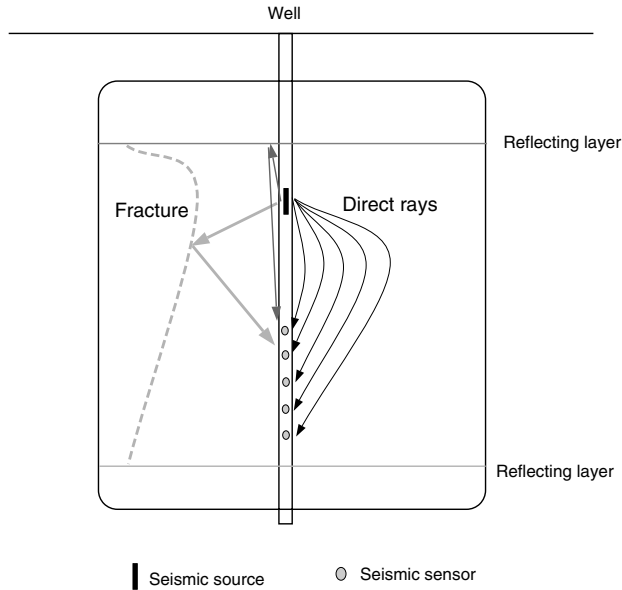
Figure 12 Wave propagation in single-well seismic data acquisition. The sketch displays the principle of wave propagation from the source to the receivers along direct or reflected raypaths.

Yet the cores did not reveal major fractures, which are expected to be present in the CO_2 injection area. A possible explanation is that the seismic velocities are governed by the pore structure and the high porosity ($\sim$50%) of the diatomite. Although the difference in wavelengths between the field data (m scale) and the ultrasonic lab data (mm scale) is considerable, both are still much larger than the pore size (μm scale), such that the sampled medium could exhibit the same degree of heterogeneity based on its pore structure. Although the introduction of hydrofractures at the field scale adds a degree of structural heterogeneity to the medium, which increases the permeability of the reservoir, it may not necessarily increase the already high porosity value. Therefore, in the case of diatomite, the seismic waves may not be as much affected by the presence of hydrofractures as by the high porosity value. This could be an explanation for the lack of evidence of the hydraulic fracture in the velocity tomograms in Figs 9 and 10. However, the time-lapse experiments shown in this study indicate the effectiveness of this method in monitoring temporal changes in the reservoir.

In summary, the results of the single-well data independently confirm the results of the cross-well experiment in the vicinity of the source well OB-C1. Therefore, when available, both experiments should be run simultaneously to determine the reliability of the velocity estimates.
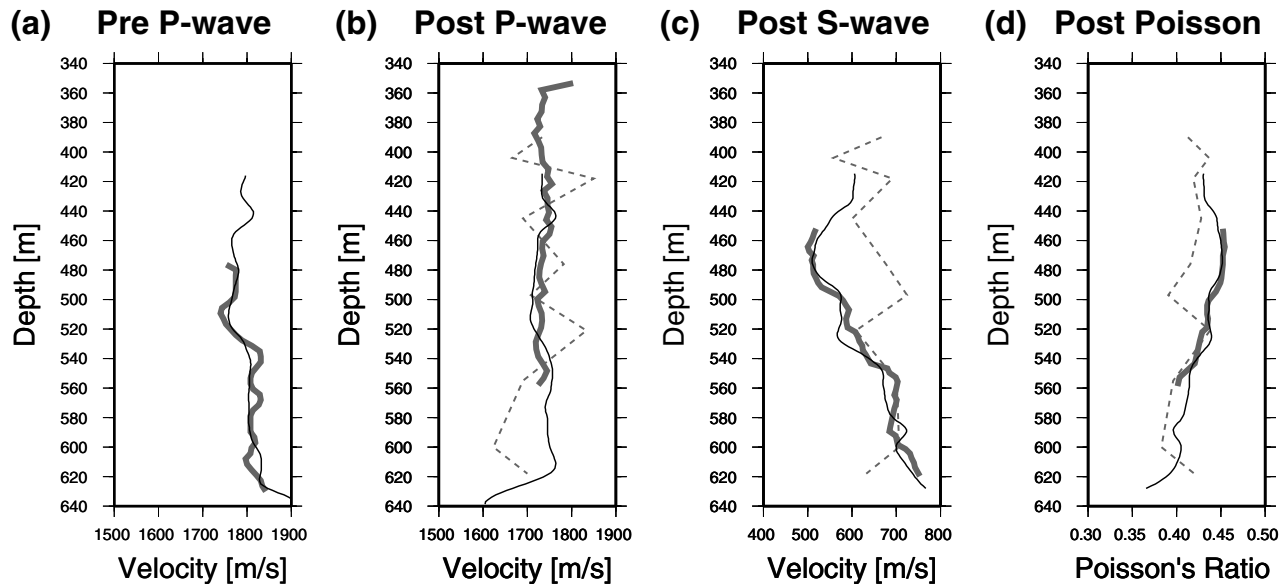
Figure 13 Comparison between cross-well and single-well estimates of the velocities and Poisson's ratio. The thin line represents a 5 m horizontal average of estimates along the source borehole from tomographic studies, while the thick line represents the results of the single-well study. The dashed line represents the results of ultrasonic measurements on cores retrieved in the vicinity of the CO_2 injection site. (a) Pre-injection P-wave estimates. (b) Post-injection P-wave estimates. (c) Post-injection S-wave estimates. (d) Post-injection Poisson's ratio.

Reflected waves

In addition to the direct wave, the single-well data revealed an additional phase that was indicated in Fig. 7, arriving between 21 and 24 ms. The possibility that this event could be a reflection off the hydrofracture between the observation wells, OB-C1 and OB-C2, was investigated. Because the moveout of the reflection is horizontal in the common-offset domain, it is unlikely that it represents a reflection of the fault as it cuts through the cross-section in Figs 9–11 at an angle. It is more likely that this event reflects off a vertical feature adjacent to the well throughout the reservoir.

To image this event and to help discriminate between external reflections and internal (borehole) multiples, common-midpoint (CMP) processing was performed. Gathers were created with a spacing of 1 m and a maximum fold of 24. A predictive deconvolution was applied followed by a mute of the direct wave. To investigate the coherence of the reflections, velocity analysis was performed. It was found that a stacking velocity of 1675 m/s resulted in maximum coherence

in the reflected data. The quality of the coherence analysis was limited because the minimum source–receiver offset (27.5 m) was much longer than the distance from the borehole to the reflector (11–13 m), leading to a long NMO stretch on the far-offset traces. The long offsets required the application of a stretch mute, and therefore the hyperbolic moveout of the reflection event is mainly defined on the near-offset traces. Further details of the processing can be found in Daley, Gritto and Majer (2003b). Two NMO-corrected CMP gathers are shown in Fig. 14.

It was difficult to use moveout analysis to discriminate between reflections from vertical features parallel to the borehole and multiples along the borehole caused by the acquisition equipment itself. The arrival time of the main event (about 4 ms after the direct arrival), however, does not correlate with the arrival time of multiples reflected between the larger equipment pieces (i.e. the source and the tube-wave suppressor are 9.1 m apart). Furthermore, the amplitude of the event varies significantly with depth, indicating that a reflection off borehole equipment is unlikely.
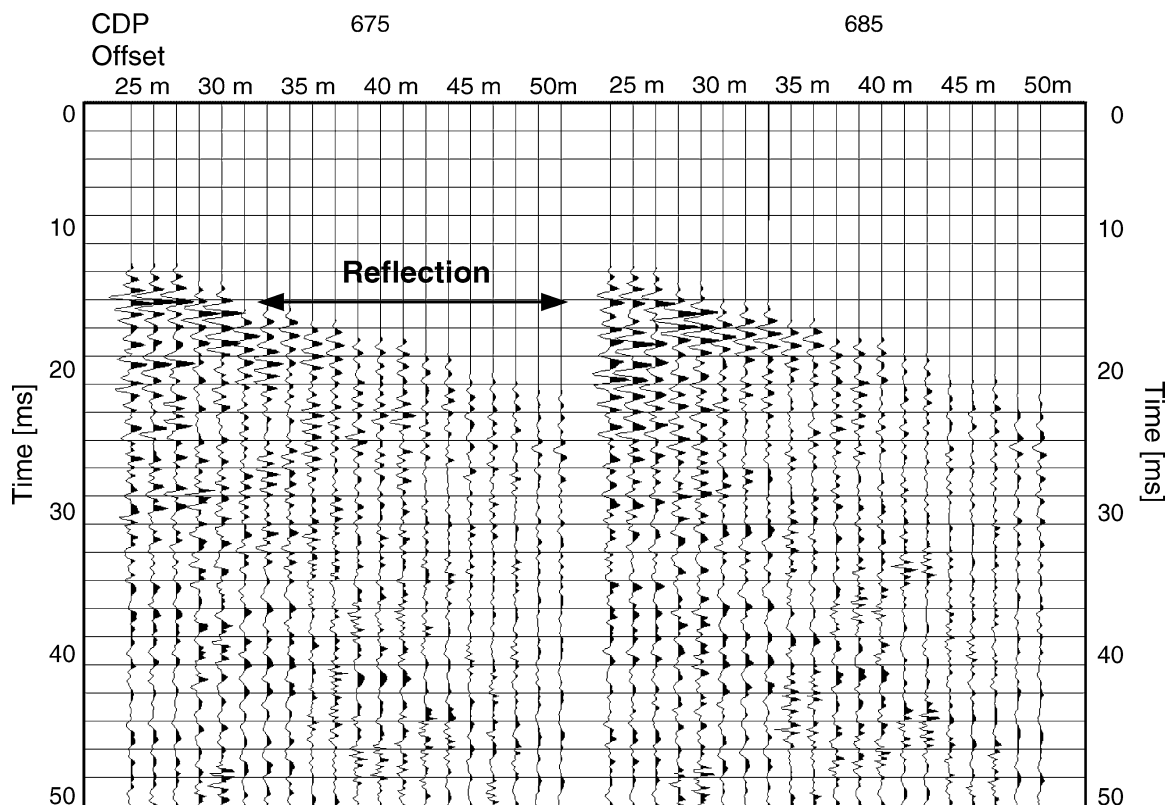
Figure 14 NMO-corrected common-midpoint gather. The data are plotted at the true amplitude value after applying spherical divergence correction.
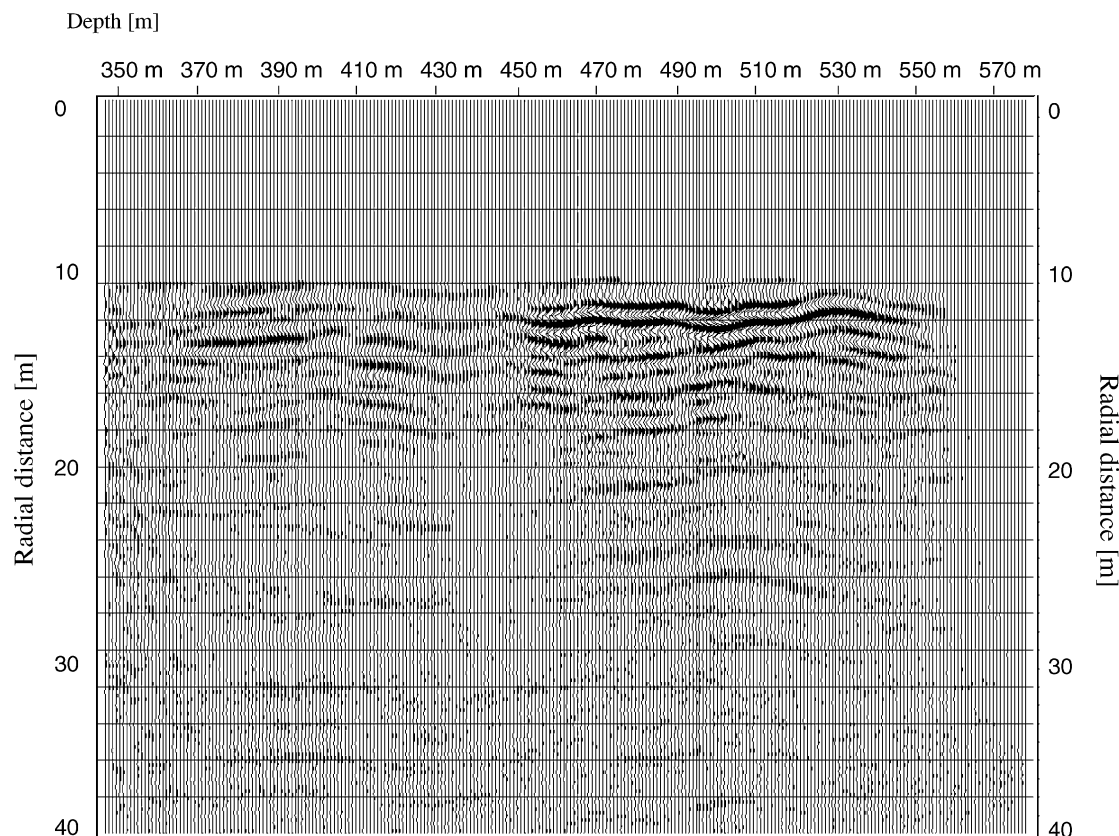
Figure 15 Results of Kirchhoff depth migration using a variable velocity field as estimated from the P-wave traveltime inversion. The traces represent 1 m (3 ft) bins. A strong reflection is visible at a radial distance of 11–13 m over a depth interval from 450 to 550 m, while a weaker event is located between 370 and 410 m depth.

The final imaging step involved a Kirchhoff depth migration using a variable P-wave velocity field as estimated by the traveltime inversion in Fig. 9(b). The result of the migration is shown in Fig. 15. A strong reflection event is visible at a radial distance of 11–13 m from the well at a depth interval between 450 and 550 m. A possible continuation of this event is visible above the injection interval between 370 and 410 m depth at the same distance from the well. The coherence of these events after migration, in combination with the change in amplitude with depth, indicates that these are formation reflections rather than borehole multiples.

To interpret these arrivals, the geometry of the injection wells is shown in Fig. 16. The two observation wells deviate, showing separate top and bottom locations. However, the deviations occur between 122 and 244 m and do not affect the measurements in the reservoir section (420–640 m) where the wells are reasonably straight, as can be seen by the source and receiver locations in Figs 9–11. The locations of the injection wells are indicated by the circles at a distance of about 12 m

and 15 m from OB-C1. The water and CO_2 injection wells are labelled 11-8W and 11-8WR, respectively. The estimated strike of the two hydrofractures, indicated by the parallel lines, was derived from surface tiltmeter measurements (Perri *et al.* 2000). The scale indicates that the event in Fig. 15 correlates in space with the location of the water-injection hydrofracture and not the CO_2 hydrofracture. However, discussions with engineers at Chevron, USA, revealed that upon CO_2 injection, the fracture 11-8W showed an increase in pressure first, suggesting that a flowpath exists for the CO_2 between the new and the old fractures. This is not unlikely, because the water flood in 11-8W has been ongoing since 1992, which has undoubtedly affected the immediate area of the hydrofracture. Similar observations of conductivity and breakthroughs between neighbouring fractures have been observed in wells adjacent to the CO_2 pilot (Perri *et al.* 2000). Thus it is possible that the event in Fig. 15 indicates the presence of the original hydrofracture 11-8W. The extension of this event to depths shallower than the injection interval indicates that the
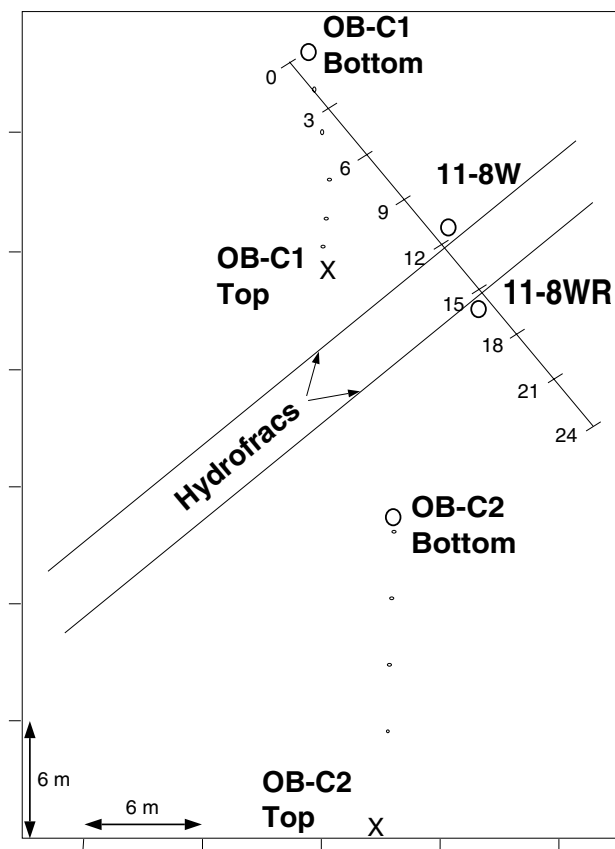
Figure 16 Geometry of the observation and injection wells. The circles at 12 m and 15 m radial distance from OB-C1 represent, respectively, the bottom of 11-8W (the original water injection well) and 11-8WR (the secondary CO_2 injection well which was drilled as a parallel section at the bottom of the original borehole 11-8W).

fracture migrated upwards in the reservoir, an occurrence that was not originally planned. A closer look at Fig. 15 may indicate a secondary arrival, around 16 m radial distance from observation well OB-C1, that correlates with the location of the CO_2 injection fracture in Fig. 16. In this case, the difference in reverberations between the two reflection events may indicate that the younger fracture has less aperture than the older one (i.e. a single fracture versus a fractured zone), which can be expected considering the history of the water injection in the past. However, the data quality is not good enough to draw a final conclusion for this hypothesis.

CONCLUSIONS

The goal of the current experiment was to investigate whether the location and migration of CO_2 or its effects in geological sequestration processes can be imaged with seismic bore-

hole methods. The time-lapse borehole experiment was conducted over a period of one year, during which a series of cross- and single-well experiments resulted in the successful acquisition of P- and S-wave data. The addition of a tube-wave suppressor during the post-injection phase of the single-well experiment resulted in the reduction of tube-wave amplitudes, such that the shear wave and the reflected waves were visible in the data records. However, the comparison of seismic amplitudes was not possible, because different receiver types were used during the pre- and post-injection phases.

The separate results of the cross-well experiments showed no clear indication of the location of the fault between the two observation holes. Differencing the P-wave velocity estimates, however, revealed the possible location in the form of an abrupt termination of a velocity anomaly. At the same time there was no evidence of the hydrofracture in the cross-well results.

The P-wave and S-wave velocity estimates showed a decrease in value over the course of the CO_2 injection phase, indicating a possible increase in pore pressure throughout the reservoir. However, using the velocity estimates alone, it was not possible to determine whether the CO_2 exists in gas form or whether it is dissolved into the liquid phase of the reservoir. After Poisson's ratio was calculated from the velocities, however, it was concluded that the CO_2 had dissolved into the liquid phase, as the time-lapse results revealed an increase in PR. This shows the advantage of simultaneous acquisition of P- and S-wave data. The tomographic images suggested the extension of the hydrofracture to a shallower section of the reservoir above the intended fracture interval.

The concurrent acquisition of single-well data enabled us to verify the results of the cross-well survey. The wavelengths excited in the single-well experiment are long enough to sample the medium in the vicinity of the well without too much interference from borehole effects as in the case of sonic logging. Therefore, the velocity estimates are more representative of the medium, and, as in our case, could be used to verify the results of the cross-well survey independently. Furthermore, the single-well data indicated the presence of a reflection event that coincided with the location of the hydrofracture between the observation wells. At the same time, no indications of the presence of the fault were observable in the single-well data.

The combination of seismic cross- and single-well experiments appears to be suitable for investigating the presence of CO_2 in subsurface reservoirs. The advantage of seismic

borehole over surface methods is a better resolution, which allows detection of the subtle changes in velocity and the spatial distribution of the effects of CO$_2$ in the subsurface. Cross-well tomography offers the advantage of imaging a larger area for integral time-lapse changes, while single-well imaging appears to be suited for direct target detection as in the case of a vertical hydrofracture. Both experiments can be readily conducted at the same time and offer the possibility of verifying common results, while they provide complementary information that adds to the general understanding of the reservoir properties.

ACKNOWLEDGEMENTS

REFERENCES

Bilodeau B.J. 1995. Determining water saturation in diatomite using wireline logs, Lost Hills Field, California. *Proceedings of the SPE/AAPG Western Regional Meeting* **SPE 29653**, 369–382.

Bourbie T., Coussy O. and Zinszner B. 1987. *Acoustics of Porous Media*. Gulf Publishing Co., Houston.

Daley T.M. and Cox D. 2001. Orbital vibrator seismic source for simultaneous P- and S-wave cross well acquisition. *Geophysics* **66**, 1471–1480.

Daley T.M., Gritto R., Majer E.L. and West P. 2003a. Tube-wave suppression in single-well seismic acquisition. *Geophysics* **68**, 863–869.

Daley T.M., Gritto R. and Majer E.L. 2003b. *Single well seismic imaging of a gas-filled hydrofracture*. Lawrence Berkeley National Laboratory Report, LBNL-53601.

Detournay E. and Cheng H. 1993. A short course on poroelasticity in rock mechanics: constitutive equations – theoretical background. *Proceedings of the 34th U.S. Rock Mechanics Symposium*, pp. 1–28.

Dvorkin J., Mavko G. and Nur A. 1999. Overpressure detection from compressional- and shear-wave data. *Geophysical Research Letters* **26**, 3417–3420.

Dvorkin J. and Nur A. 1996. Elasticity of high-porous sandstones: Theory for two North Sea data sets. *Geophysics* **61**, 1363–1370.

Graham S.A. and Williams L.A. 1985. Tectonic, depositional and diagenetic history of Monterey formation (Miocene), central San Joaquin basin, California. *AAPG Bulletin* **69**, 385–411.

Hoversten G.M., Gritto R., Washbourne J. and Daley T.M. 2003. CO$_2$ gas/oil ratio prediction in a multi-component reservoir by combined seismic and electromagnetic imaging. *Geophysics* **68**, 1580–1591.

Isaacs C.M. 1982. Influence of rock composition on the kinetics of silica phase changes in the Monterey Formation, Santa Barbara area, California. *Geology* **10**, 304.

Majer E.L., Peterson J.E., Daley T.M., Kaelin B., Queen J., D'Onfro P. and Rizer W. 1997. Fracture detection using cross well and single well surveys. *Geophysics* **62**, 495–504.

Mallick S. 2001. AVO and elastic impedance. *The Leading Edge* **20**, 1094–1104.

Meredith J.A., Toksöz M.N. and Cheng C.H. 1993. Secondary shear waves from source boreholes. *Geophysical Prospecting* **41**, 287–312.

Perri P.A., Emanuele M.A., Fong W.S. and Morea M.F. 2000. Lost Hills CO$_2$ pilot: evaluation, design, injectivity test results and implementation. *Proceedings of the SPE/AAPG Western Regional Meeting* **SPE 62526**, 13.

Peterson J.E., Paulson B.N. and McEvilly T.V. 1985. Applications of algebraic reconstruction techniques to cross hole seismic data. *Geophysics* **50**, 1566–1580.

Simpson G. 2001. Influence of compression-induced fluid pressures on rock strength in the brittle crust. *Journal of Geophysical Research* **106**(B9), 19465–19478.

Wang Z., Cates M.E. and Langan R.T. 1998. Seismic monitoring of a CO$_2$ flood in a carbonate reservoir: a rock physics study. *Geophysics* **63**, 1604–1617.